

Initial results of NEXT-DEMO, a large-scale prototype of the NEXT-100 experiment

The NEXT Collaboration

V. Álvarez,^a F.I.G. Borges,^b S. Cárcel,^a J. Castel,^c S. Cebrián,^c A. Cervera,^a
 C.A.N. Conde,^b T. Dafni,^c T.H.V.T. Dias,^b J. Díaz,^a M. Egorov,^d R. Esteve,^e
 P. Evtoukhovitch,^f L.M.P. Fernandes,^b P. Ferrario,^a A.L. Ferreira,^g E.D.C. Freitas,^b
 V.M. Gehman,^d A. Gil,^a A. Goldschmidt,^d H. Gómez,^c J.J. Gómez-Cadenas,^{a*}
 D. González-Díaz,^c R.M. Gutiérrez,^h J. Hauptman,ⁱ J.A. Hernando Morata,^j
 D.C. Herrera,^c F.J. Iguaz,^c I.G. Irastorza,^c M.A. Jinete,^h L. Labarga,^k A. Laing,^a
 I. Liubarsky,^a J.A.M. Lopes,^b D. Lorca,^a M. Losada,^h G. Luzón,^c A. Marí,^e
 J. Martín-Albo,^{a†} A. Martínez,^a T. Miller,^d A. Moiseenko,^f F. Monrabal,^{a‡}
 C.M.B. Monteiro,^b F.J. Mora,^e L.M. Moutinho,^g J. Muñoz Vidal,^a H. Natal da Luz,^b
 G. Navarro,^h M. Nebot-Guinot,^a D. Nygren,^d C.A.B. Oliveira,^d R. Palma,^l J. Pérez,^k
 J.L. Pérez Aparicio,^l J. Renner,^d L. Ripoll,^m A. Rodríguez,^c J. Rodríguez,^a
 F.P. Santos,^b J.M.F. dos Santos,^b L. Seguí,^c L. Serra,^a D. Shuman,^d A. Simón,^a
 C. Sofka,ⁿ M. Sorel,^a J.F. Toledo,^d A. Tomás,^c J. Torrent,^m Z. Tsamalaidze,^f
 D. Vázquez,^j J.F.C.A. Veloso,^g J.A. Villar,^c R. Webb,ⁿ J.T. White,ⁿ N. Yahlali^a

- ^a *Instituto de Física Corpuscular (IFIC), CSIC & Universitat de València
Calle Catedrático José Beltrán, 2, 46980 Paterna, Valencia, Spain*
- ^b *Departamento de Física, Universidade de Coimbra
Rua Larga, 3004-516 Coimbra, Portugal*
- ^c *Lab. de Física Nuclear y Astropartículas, Universidad de Zaragoza
Calle Pedro Cerbuna, 12, 50009 Zaragoza, Spain*
- ^d *Lawrence Berkeley National Laboratory (LBNL)
1 Cyclotron Road, Berkeley, California 94720, USA*
- ^e *Instituto de Instrumentación para Imagen Molecular (I3M), Universitat Politècnica de València
Camino de Vera, s/n, Edificio 8B, 46022 Valencia, Spain*
- ^f *Joint Institute for Nuclear Research (JINR)
Joliot-Curie 6, 141980 Dubna, Russia*
- ^g *Institute of Nanostructures, Nanomodelling and Nanofabrication (i3N), Universidade de Aveiro
Campus de Santiago, 3810-193 Aveiro, Portugal*
- ^h *Centro de Investigaciones, Universidad Antonio Nariño
Carretera 3 este No. 47A-15, Bogotá, Colombia*
- ⁱ *Department of Physics and Astronomy, Iowa State University
12 Physics Hall, Ames, Iowa 50011-3160, USA*
- ^j *Instituto Gallego de Física de Altas Energías (IGFAE), Univ. de Santiago de Compostela
Campus sur, Rúa Xosé María Suárez Núñez, s/n, 15782 Santiago de Compostela, Spain*
- ^k *Departamento de Física Teórica, Universidad Autónoma de Madrid
Ciudad Universitaria de Cantoblanco, 28049 Madrid, Spain*
- ^l *Dpto. de Mecánica de Medios Continuos y Teoría de Estructuras, Univ. Politècnica de València
Camino de Vera, s/n, 46071 Valencia, Spain*
- ^m *Escola Politècnica Superior, Universitat de Girona
Av. Montilivi, s/n, 17071 Girona, Spain*
- ⁿ *Department of Physics and Astronomy, Texas A&M University
College Station, Texas 77843-4242, USA*

E-mail: justo.martin-albo@ific.uv.es, francesc.monrabal@ific.uv.es

ABSTRACT: NEXT-DEMO is a large-scale prototype of the NEXT-100 detector, an electroluminescent time projection chamber that will search for the neutrinoless double beta decay of ^{136}Xe using 100–150 kg of enriched xenon gas. NEXT-DEMO was built to prove the expected performance of NEXT-100, namely, energy resolution better than 1% FWHM at 2.5 MeV and event topological reconstruction. In this paper we describe the prototype and its initial results. A resolution of 1.75% FWHM at 511 keV (which extrapolates to 0.8% FWHM at 2.5 MeV) was obtained at 10 bar pressure using a gamma-ray calibration source. Also, a basic study of the event topology along the longitudinal coordinate is presented, proving that it is possible to identify the distinct dE/dx of electron tracks in high-pressure xenon using an electroluminescence TPC.

KEYWORDS: Time projection chambers (TPC); Gaseous imaging and tracking detectors.

*Spokesperson (gomez@mail.cern.ch)

†Co-corresponding author

‡Co-corresponding author

Contents

1. Introduction	1
2. The NEXT-DEMO prototype	2
2.1 Gas system	4
2.2 Pressure vessel	6
2.3 Time projection chamber	7
2.4 Detection planes	8
2.5 Electronics and DAQ	9
3. Analysis of ^{22}Na gamma-ray data	10
3.1 Calibration of the photomultipliers	12
3.2 Waveforms processing and event selection	12
4. Primary signals in NEXT-DEMO	14
5. Energy resolution analysis	16
6. The topological signature	19
7. Summary and outlook	22

1. Introduction

The NEXT-100 [1] time projection chamber (TPC), currently under construction, will search for neutrinoless double beta decay ($\beta\beta 0\nu$) using 100–150 kg of xenon gas enriched in the ^{136}Xe isotope to 91%. The detector boasts two important features for $\beta\beta 0\nu$ searches: *excellent energy resolution* (better than 1% FWHM at the Q value of ^{136}Xe) and event *topological information* for the identification of signal and background. This combination gives NEXT an excellent experimental sensitivity to $\beta\beta 0\nu$ [2]. In addition, the technique can be extrapolated to the ton-scale, thus allowing the full exploration of the inverted hierarchy of neutrino masses [3].

Xenon, as a detection medium, provides both *scintillation* and *ionization* as primary signals. The former is used in NEXT to establish the start-of-event time (t_0), while the latter is used for calorimetry and tracking. In its gaseous phase, xenon can provide high energy resolution, in principle as good as 0.3% FWHM at the Q value of ^{136}Xe [4]. In order to achieve optimal energy resolution, the ionization signal is amplified in NEXT using the *electroluminescence* (EL) of xenon: the electrons liberated by ionizing particles passing through the gas are first drifted towards the TPC anode by a weak electric field (~ 300 V/cm), entering then into another region where they are accelerated by a high electric field (~ 25 kV/cm at 10 bar), intense enough so that the electrons can

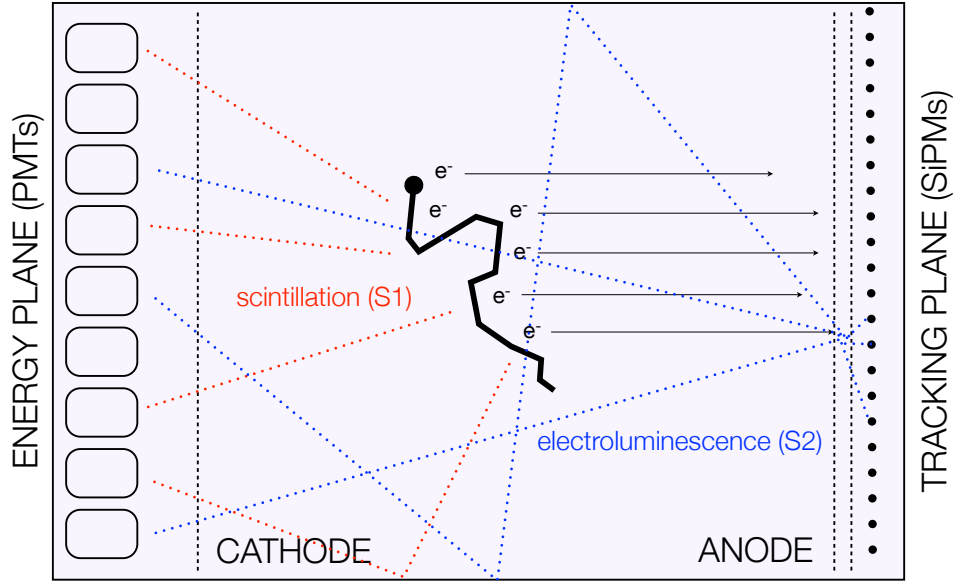


Figure 1. The *Separated, Optimized Functions* (SOFT) concept in the NEXT experiment: EL light generated at the anode is recorded in the photosensor plane right behind it and used for tracking; it is also recorded in the photosensor plane behind the transparent cathode and used for a precise energy measurement.

excite the xenon atoms but not enough to ionize them. This excitation energy is ultimately released in the form of proportional (with sub-poissonian fluctuations) *secondary scintillation* light.

NEXT-100 will have different readout systems for calorimetry and tracking (see figure 1). An array of photomultiplier tubes (PMTs), the so-called *energy plane*, located behind the TPC cathode detects a fraction of the secondary scintillation (S2) light to provide a precise measurement of the total energy deposited in the gas. These PMTs detect as well the primary scintillation (S1), used to signal the start of the event. The forward-going S2 light is detected by a dense array of silicon photomultipliers (SiPMs), known as the *tracking plane*, located behind the anode, very close to the EL region, and is used for event topological reconstruction.

During the last three years, as part of the NEXT R&D program, we have built the NEXT-DEMO prototype with the double aim of demonstrating the NEXT detector concept and gaining experience that would facilitate the design, construction and operation of the NEXT-100 detector. This paper describes the prototype and presents the results of the initial operation. The organization is as follows: section 2 describes in detail the apparatus; section 3 explains its characterization with a ^{22}Na source; section 5 presents our initial energy resolution analysis, and section 6 first results on topology reconstruction; section 7 concludes.

2. The NEXT-DEMO prototype

NEXT-DEMO, shown in figure 2, is a high-pressure xenon electroluminescent TPC implementing the NEXT detector concept described above. Its active volume is 30 cm long and 30 cm diameter. A tube of hexagonal cross section made of PTFE is inserted into the active volume to improve the

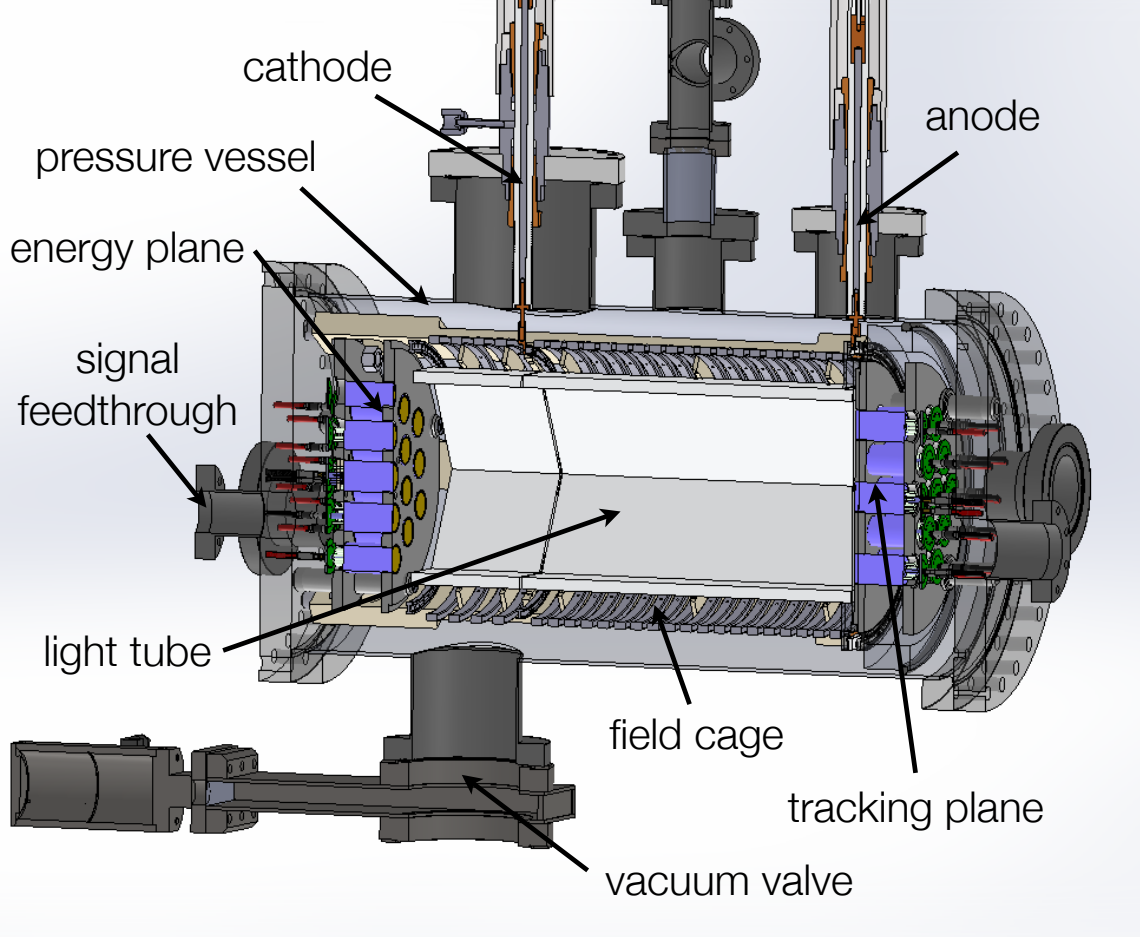


Figure 2. Cross-section drawing of the NEXT-DEMO detector with all major parts labelled.

light collection. The TPC is housed in a stainless-steel pressure vessel that can withstand up to 15 bar. Natural xenon circulates in a closed loop through the vessel and a system of purifying filters. The detector is not radiopure and is not shielded against natural radioactivity. It is installed in a semi-clean room (see figure 3) at the *Instituto de Física Corpuscular* (IFIC), in Valencia, Spain.

The main objective of NEXT-DEMO was the validation of the NEXT-100 design. More specifically, the goals of the prototype were the following: (a) to demonstrate good energy resolution in a large active volume; (b) to reconstruct the topological signature of electrons in high-pressure xenon gas (HPXe); (c) to test long drift lengths and high voltages; (d) to understand gas recirculation and purification in a large volume, including operation stability and robustness against leaks; and (e) to understand the collection of light and the use of wavelength shifters (WLS).

In this paper we describe the initial operation of NEXT-DEMO with a tracking plane implemented using 19 pressure-resistant photomultipliers, identical to those used in the energy plane but operated at a lower gain. Instrumenting the tracking plane with PMTs — unlike NEXT-100, which will use SiPMs — during this period simplified the initial commissioning, debugging and operation of the detector due to the smaller number of readout channels (19 PMTs in contrast to the 256 SiPMs projected for the second phase of NEXT-DEMO) and their intrinsic sensitivity to the UV



Figure 3. The NEXT-DEMO detector and ancillary systems (gas system, front-end electronics and DAQ) in their location at a semi-clean room at IFIC.

light emitted by xenon.

The detector response was studied under two different conditions: an *ultraviolet configuration* (UVC) in which the PTFE *light tube* had no coating, and a *blue configuration* (BC) in which the panels were coated with *tetraphenyl butadiene* (TPB), a wavelength shifter, in order to study the possible improvement in light collection.

In the rest of the section we describe the major parts of the NEXT-DEMO detector.

2.1 Gas system

The functions of the gas system of NEXT-DEMO are the evacuation of the detector, its pressurization and depressurization with xenon (and argon), and the recirculation of the gas through purification filters. A schematic of the system is shown in figure 4.

The standard procedure during normal operation of the detector starts with the evacuation of the vessel to vacuum levels around 10^{-5} mbar, followed by an argon purge. A second vacuum step exhausts the argon from the system. The detector is then filled with xenon gas to pressures up to 15 bar. The xenon can be cryogenically reclaimed to a stainless-steel bottle connected to the gas system by simply immersing this in a dewar filled with liquid nitrogen. The pressure regulator of the bottle is fully opened to allow the xenon gas to flow inside it (due to the temperature difference) and freeze.

The vacuum pumping system consists of a roughing pump (Edwards XDS5 scroll vacuum pump) and a turbo molecular pump (Pfeiffer HiPace 300). Vacuum pressures better than 10^{-7} mbar

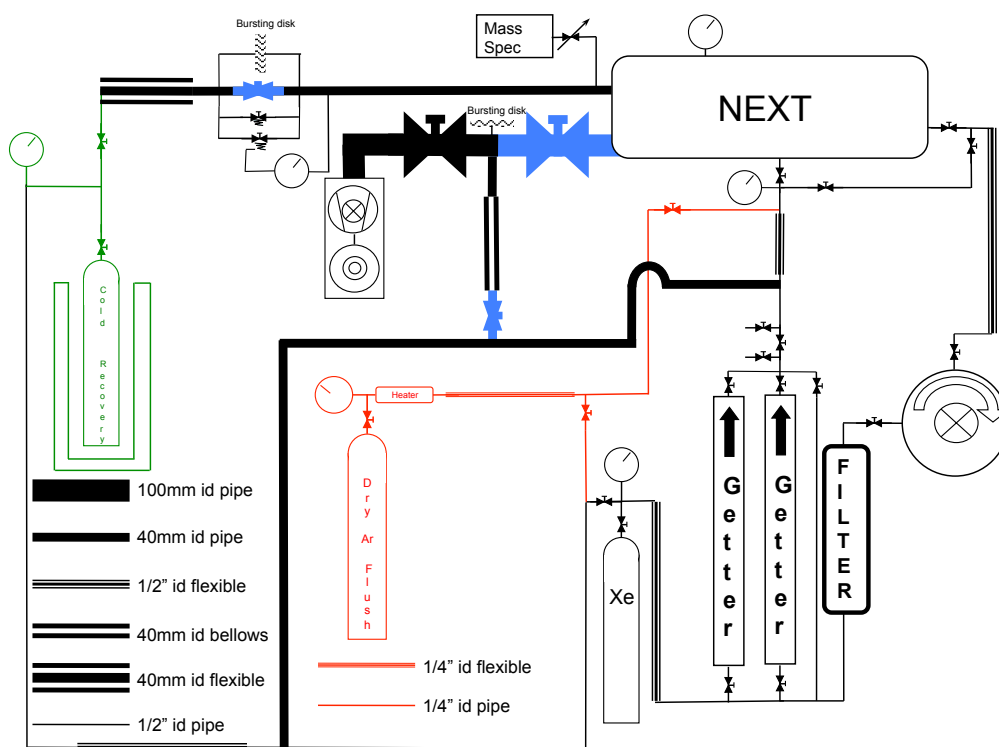


Figure 4. Simplified schematic of the gas system of NEXT-DEMO.

have been obtained after pumping out the detector for several days. The recirculation loop is powered by an oil-less, single-diaphragm compressor (KNF PJ24999-2400) with a nominal flow of 100 standard liters per minute. This translates to an approximate flow of 10 liters per minute at 10 bar, thus recirculating the full volume of NEXT-DEMO (~ 45 L) in about 5 minutes. The gas system is equipped with both room-temperature (SAES MC50) and heated *getters* (SAES PS4-MT15) that remove electronegative impurities (O_2 , H_2O , etc.) from the xenon. All the gas piping, save for the inlet gas hoses and getter fittings, are 1/2 inch diameter with VCR fittings. A set of pressure relief valves (with different settings for the various parts of the system) and a burst disk in the vacuum system protect the equipment and personnel from overpressure hazards.

The operation of the gas system has been, in general, very stable. The detector has run without interruption for long periods of up to 6 weeks with no leaks and continuous purification of the gas. However, one major leak occurred when the diaphragm of the recirculation pump broke, causing the loss of the xenon volume contained in the chamber. To avoid the same type of accident, we installed an emergency mechanism that, on pressure drop, automatically closes several valves to insulate the pump from the rest of the gas system. This device avoided another important gas loss when the diaphragm of the pump broke a second time. After those two accidents the system has run without major issues, although identifying and fixing micro-leaks has been a rather involved task.

Several lessons that can be applied to the gas system of NEXT-100 have been learned. The most important one is the need for a robust and reliable pump in order to minimize the probability of any gas loss during the operation of the expensive enriched xenon. Concerning the getters, we

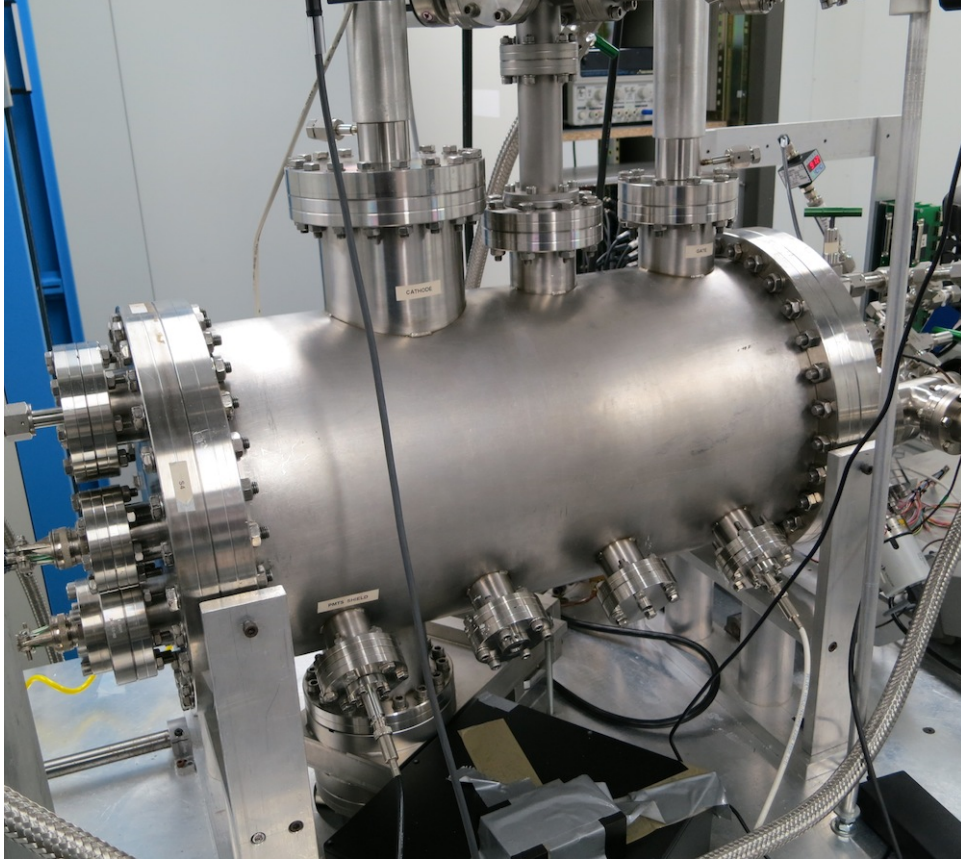


Figure 5. The pressure vessel of NEXT-DEMO.

have confirmed that room-temperature getters emit radon, while emanation from hot getters appears to be negligible.

2.2 Pressure vessel

The pressure vessel of NEXT-DEMO, shown in figure 5, is a stainless-steel (grade 304L) cylindrical shell, 3 mm thick, 30 cm diameter and 60 cm length, welded to CF flanges on both ends. The two end-caps are 3-cm thick plates with standard CF knife-edge flanges. Flat copper gaskets are used as sealing. The vessel was certified to 15 bar operational pressure. It was designed at IFIC and built by Trinos Vacuum Systems, a local manufacturer. Additional improvements — including the support structure and a rail system to open and move the end-caps — have been made using the mechanical workshop at IFIC.

The side of the chamber includes 8 CF40 half-nipples. One set of 4 is located in the horizontal plane while the other is displaced towards the underside with respect to the first set by 60° . These contain radioactive source ports used for calibration of the TPC. The ports are made by welding a 0.5 mm blank at the end of a 12 mm liquid feedthrough. On top of the vessel and along the vertical plane there are three additional half-nipples (CF130, CF67 and CF80) used for high-voltage feeding and connection to a mass spectrometer (through a leak valve). On the opposite side, at the bottom, a CF100 port connects the pressure vessel to the vacuum pumping system. A guillotine valve closes

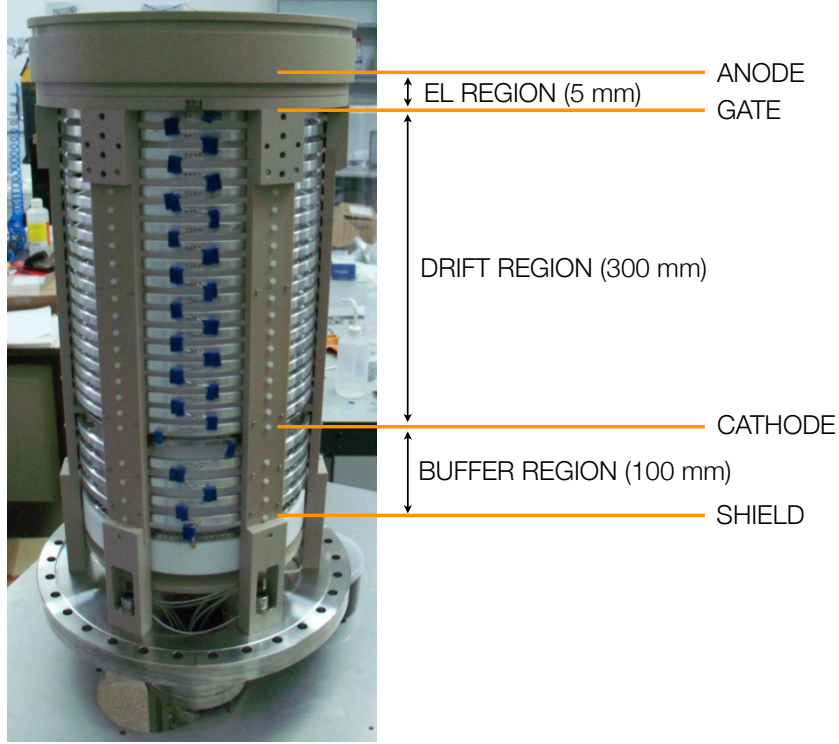


Figure 6. External view of the time projection chamber mounted on one end-cap. The approximate positions of the different regions of the TPC are indicated.

this connection when the vessel is under pressure. The end-caps include several CF ports for the connections to the gas recirculation loop and for the feedthroughs (power and signal) of the PMT planes.

2.3 Time projection chamber

Three metallic wire grids — called *cathode*, *gate* and *anode* — define the two active regions of the chamber (see figure 6): the 30-cm long *drift region*, between cathode and gate; and the 0.5-cm long *EL region*, between gate and anode. Gate and anode were built using stainless-steel meshes with 88% open area (30- μ m diameter wires, 50 wires/inch) clamped in a tongue-and-groove circular frame with a tensioning ring that is torqued with set screws to achieve the optimum tension. The cathode was built in a similar fashion by clamping parallel wires 1 cm apart into another circular frame.

The electric field in the TPC is created by supplying a large negative voltage to the cathode, then degrading it using a series of metallic rings of 30 cm diameter spaced 5 mm and connected via 0.5 G Ω resistors. The rings were manufactured by cutting and machining aluminum pipe. The gate is at negative voltage so that a moderate electric field — typically of 2.5 to 3 kV cm⁻¹ bar⁻¹ — is created between the gate and the anode, which is at ground. A *buffer region* of 10 cm between the cathode and the energy plane protects this from the high-voltage by degrading it safely to ground potential.

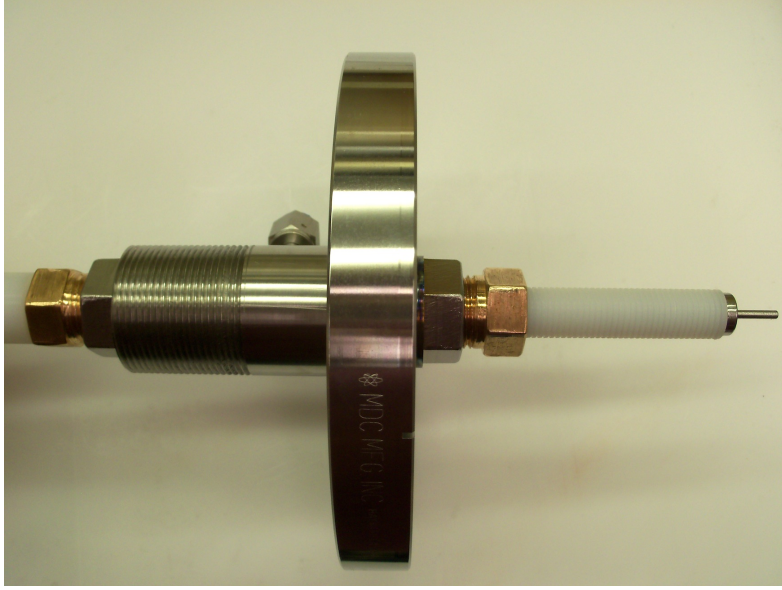


Figure 7. The NEXT-DEMO high-voltage feed-through, designed and built by Texas A&M.

The high voltage is supplied to the cathode and the gate through custom-made high-voltage feed-throughs (HVFT), shown in figure 7, built pressing a stainless-steel rod into a Tefzel (a plastic with high dielectric strength) tube, which is then clamped using plastic ferrules to a CF flange. They have been tested to high vacuum and 100 kV without leaking or sparking.

A set of six panels made of PTFE (Teflon) are mounted inside the electric-field cage forming a *light tube* of hexagonal cross section (see figure 8) with an apothem length of 8 cm. PTFE is known to be an excellent reflector in a wide range of wavelengths [5], thus improving the light collection efficiency of the detector. In a second stage, the panels were vacuum-evaporated with TPB — which shifts the UV light emitted by xenon to blue (~ 430 nm) — in order to study the improvement in reflectivity and light detection. Figure 8 (right panel) shows the light tube illuminated with a UV lamp after the coating.

Six bars manufactured from PEEK, a low outgassing plastic, hold the electric-field cage and the energy plane together. The whole structure is attached to one of the end-caps using screws, and introduced inside the vessel with the help of a rail system. All the TPC structures and the HVFT were designed and built by Texas A&M.

2.4 Detection planes

In NEXT-DEMO, the energy plane (see figure 9, left panel) is equipped with 19 Hamamatsu R7378A photomultiplier tubes. These are 1-inch, pressure-resistant (up to 20 bar) PMTs with acceptable quantum efficiency ($\sim 15\%$) in the VUV region. The resulting photocathode coverage of the energy plane is about 39%. The PMTs are inserted into a PTFE holder following a hexagonal pattern. A grid, known as *shield* and similar to the cathode but with the wires spaced 0.5 cm apart, is screwed on top of the holder and set to electrical ground. As explained above, this protects the PMTs from the high-voltage set in the cathode, and ensures that the electric field in the 10-cm buffer region is below the EL threshold.

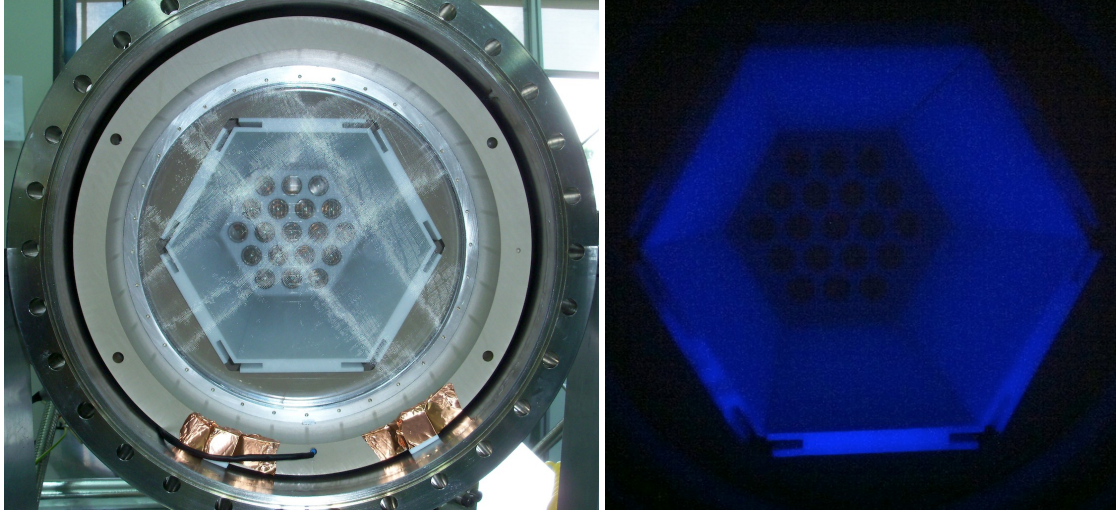


Figure 8. View of the light tube from the position of the tracking plane. Left: The meshes of the EL region can be seen in the foreground, and in the background, at the end of the light tube, the PMTs of the energy plane are visible. Right: The light tube of NEXT-DEMO illuminated with a UV lamp after being coated with TPB.

The PMTs are connected to custom-made electrical bases that are used as voltage dividers, and also allow the extraction of the signal induced in the PMTs. This requires a total of 38 cables inside the pressure vessel connected via feed-throughs.

We mentioned already that the first tracking plane of the NEXT-DEMO detector also uses 19 Hamamatsu R7378A PMTs, as shown in figure 9 (right), but operated at lower gain. They are also held by a PTFE honeycomb, mirroring the energy plane. The PMT windows are located 2 mm away from the anode mesh. Position reconstruction is based on energy sharing between the PMTs, being therefore much better than the distance between PMTs (35 mm from center to center).

Operation of the PMT planes has been in general quite stable, although shorts and broken connections appeared in some of them after the initial installation.

2.5 Electronics and DAQ

The two optical, primary signals in the NEXT detector concept are in very different scales, and the photomultipliers and their front-end electronics must be ready to handle both. Primary scintillation results in weak (a few photoelectrons per photomultiplier) and fast (the bulk of the signal comes in about 20 ns) signals, whereas the secondary scintillation — that is, the EL-amplified ionization — is intense (hundreds to thousands of photoelectrons per PMT) and slow (several microseconds long).

The gain of the PMTs in NEXT-DEMO was adjusted to around 5×10^6 for the energy plane to place the mean amplitude of a single photoelectron pulse well above electronic system noise, and approximately half that for the tracking plane since they record the direct secondary-scintillation light produced in the EL region.

The main function of the front-end electronics is to shape and filter the fast signals produced by the PMTs (less than 5 ns wide) to match the digitizer sampling rate and eliminate high frequency noise which produces unwanted ringing. An integrator is implemented by simply adding a capacitor

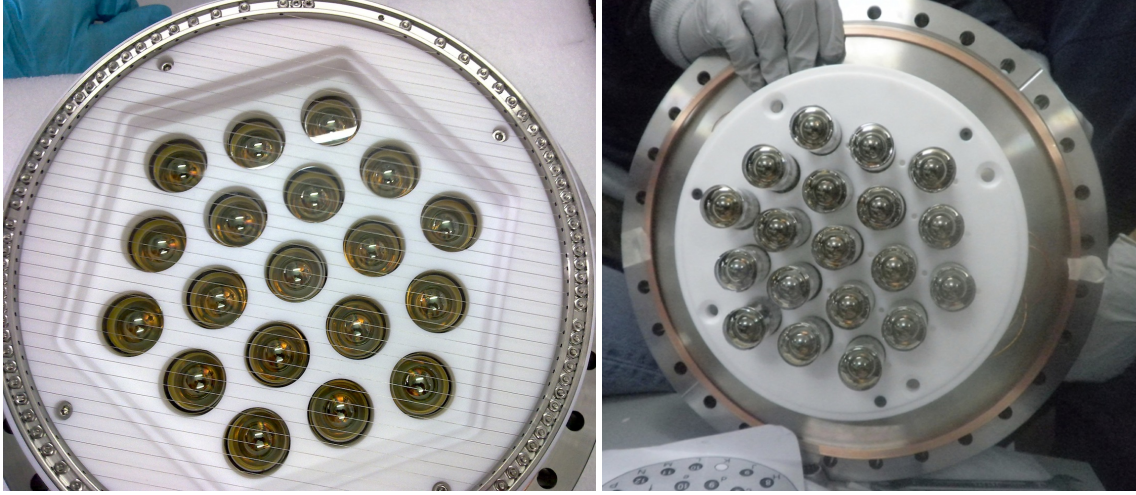


Figure 9. The energy (left) and tracking (right) planes of NEXT-DEMO, each one equipped with 19 Hamamatsu R7378A PMTs.

and a resistor to the PMT base. The charge integration capacitor shunting the anode stretches the pulse and reduces the primary signal peak voltage accordingly. Our design uses a single amplification stage based on a fully differential amplifier THS4511, which features low noise ($2 \text{ nV}/\sqrt{\text{Hz}}$) and provides enough gain to compensate for the attenuation in the following stage. Amplification is followed by a passive RC filter with a cut frequency of 800 kHz. This filtering produces enough signal stretching to allow the acquisition of many samples per single photo-electron at 40 MHz. The front-end circuit for NEXT-DEMO was implemented in 7 channel boards and connected via HDMI cables to 12-bit 40-MHz digitizer cards. These digitizers are read out by the FPGA-based DAQ modules (FEC cards) that buffer, format and send event fragments to the DAQ PCs. As for the FEC card, the 16-channel digitizer add-in card was designed in a joint effort between CERN and the NEXT Collaboration within the RD-51 program [6]. These two cards are edge mounted to form a standard 6U220 mm Eurocard. An additional FEC module with a different plug-in card is used as trigger module. Besides forwarding a common clock and commands to all the DAQ modules, it receives trigger candidates from the DAQ modules, runs a trigger algorithm in the FPGA and distributes a trigger signal. The trigger electronics also accepts external triggers for detector calibration purposes.

3. Analysis of ^{22}Na gamma-ray data

The response of the NEXT-DEMO detector was studied using a $1\text{-}\mu\text{Ci}$ ^{22}Na calibration source placed at the port near the TPC cathode. Sodium-22 is a long-lived β^+ radioactive isotope, and the annihilation of the positron emitted in its decay, which rarely travels more than 1 mm, results in two back-to-back 511-keV gammas. We used as a trigger the coincident detection of the forward gamma in the TPC and of the backward gamma in an external NaI scintillator coupled to a photomultiplier (see figure 10). This arrangement optimized the acquisition of useful calibration data.

Two data sets are discussed in this paper — one for the *ultraviolet configuration* (UVC), taken during February 2012, and another for the *blue configuration* (BC), taken during April 2012. The

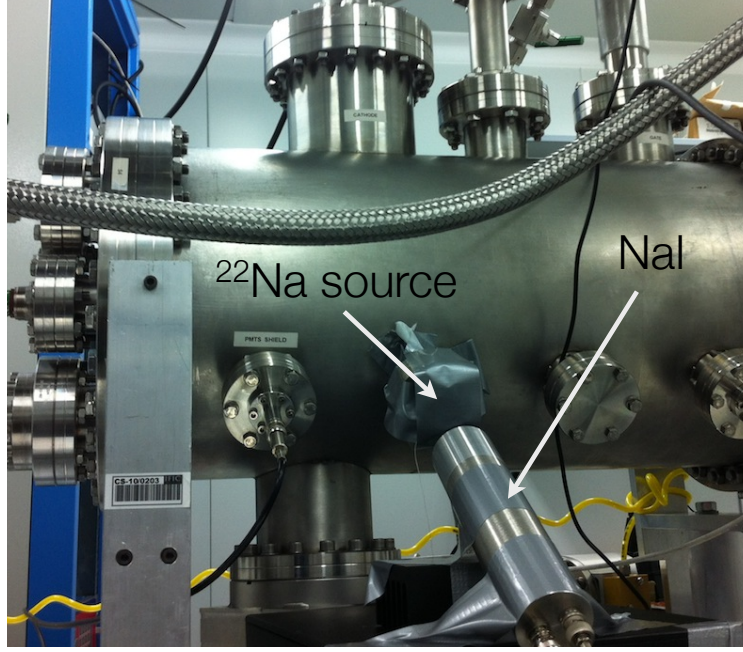


Figure 10. A view of NEXT-DEMO with the ^{22}Na calibration source installed in the port closest to the TPC cathode with the NaI scintillator used for event tagging visible in the foreground.

detector was constantly operated throughout both periods at a pressure of 10.0 bar. Nevertheless, a micro-leak that appeared during the BC period — the system was losing ~ 0.01 bar of pressure every two days — forced us to refill the chamber a number of times, and, eventually, evacuate it to fix the leaking piece (a connection in the gas system). The TPC cathode was held at -32 kV and the gate at -12 kV, resulting in a drift field of $667 \text{ V} \cdot \text{cm}^{-1}$ and an EL field of $2.4 \text{ kV} \cdot \text{cm}^{-1} \cdot \text{bar}^{-1}$. Operation was smooth in general, although occasional sparks in the EL region (due to dust on the grids or corona discharge) were not uncommon. The spark rate tended to decrease as the gas became cleaner and the dust specks were burned by previous sparks, until reaching a rate of about one spark every few days, introducing very little distortion in the data taking.

During the UVC period, the S1 signals (primary scintillation) were not sufficiently intense to be used as an efficient trigger. Instead, the detector was triggered on the delayed coincidence between a signal in the NaI and an S2 signal (secondary scintillation) in the central PMT of the energy plane up to $400 \mu\text{s}$ later (a complete drift length plus a margin). Both signals were required to be above certain thresholds (~ 150 photoelectrons for the S2) to ensure that they corresponded to the detection of the 511-keV gammas. In addition, the S2 signal had to stay above that threshold for at least $0.5 \mu\text{s}$ and at most $10 \mu\text{s}$. This last requirement was meant to reject the abundant high-energy events, most probably atmospheric muons. The trigger rate with this particular set of conditions was 1.5 Hz, consistent with the rate expected from the (weak) calibration source according to our detector simulation. Triggering on the S2 signal demanded that a long ($450 \mu\text{s}$) pre-trigger section of the PMT waveforms (buffered by the front-end electronics) be saved to allow the location of the S1 signals (which always precede the S2) during the offline data analysis.

The higher intensity of the S1 signals under the BC and several improvements in the *firmware*

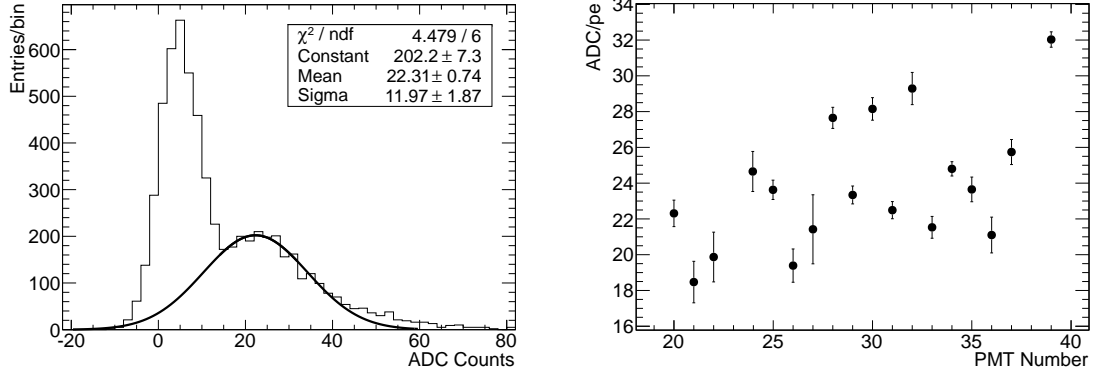


Figure 11. Left: Typical single photoelectron spectrum of one of the energy-plane photomultipliers. The single photoelectron peak is clearly separated from the background peak and can be fitted to a gaussian to measure the operating gain and charge resolution of the PMT. The non-gaussian tail on the right side of the peak is due to two-photoelectron events. Right: Gain of the 19 PMTs in the NEXT-DEMO energy plane.

of the front-end electronics made it possible to trigger the detector during the second period on the coincidence (within 25 ns) of a NaI signal and an S1 in the energy plane. The integrated charge of the S1 was required to be in the range of 1 to 20 photoelectrons. Under these conditions the trigger rate rose to 2.5 Hz. However, the data size shrank by a factor of 2, since the long pre-trigger was no longer required.

3.1 Calibration of the photomultipliers

The 19 photomultiplier tubes in the energy plane were operated at a gain of around 5×10^6 . The exact gains of the PMTs were measured using a blue LED installed in the tracking plane to illuminate the energy plane with dim light so that only single photoelectron (*spe*) pulses could be recorded. The recorded *spe* spectrum of each PMT was then fitted to a gaussian to obtain the actual gain, including the conversion factor of the digitization, as illustrated in figure 11. This procedure was repeated regularly during the operation of NEXT-DEMO with no notable changes in the gains of the PMTs.

The photomultipliers of the tracking plane were operated at a lower gain, $\sim 2 \times 10^6$, to avoid saturation (they receive much more light, being closer to the EL region). At this lower gain, it was not possible to separate the *spe* peak from the background using the procedure described above. Therefore, the gain of the PMTs at the operating voltage was measured with an oscilloscope in a black box prior to their introduction into the chamber. Their behavior during the run was monitored periodically by comparing the relative positions of the peaks in their individual recorded spectra. This proved to be sufficient since these PMTs were not used to measure the energy of the event.

3.2 Waveforms processing and event selection

The recorded raw data — that is, the individual PMT *waveforms* in ADC counts — were processed in a series of steps. First, ADC pedestals were subtracted for all individual waveforms. The pedestal level was computed for each channel and each event using the first 10000 samples in a waveform that were not considered statistical outliers. Second, using the (channel-dependent) gain calibration constants obtained with the methods described in the previous section, the pedestal-subtracted

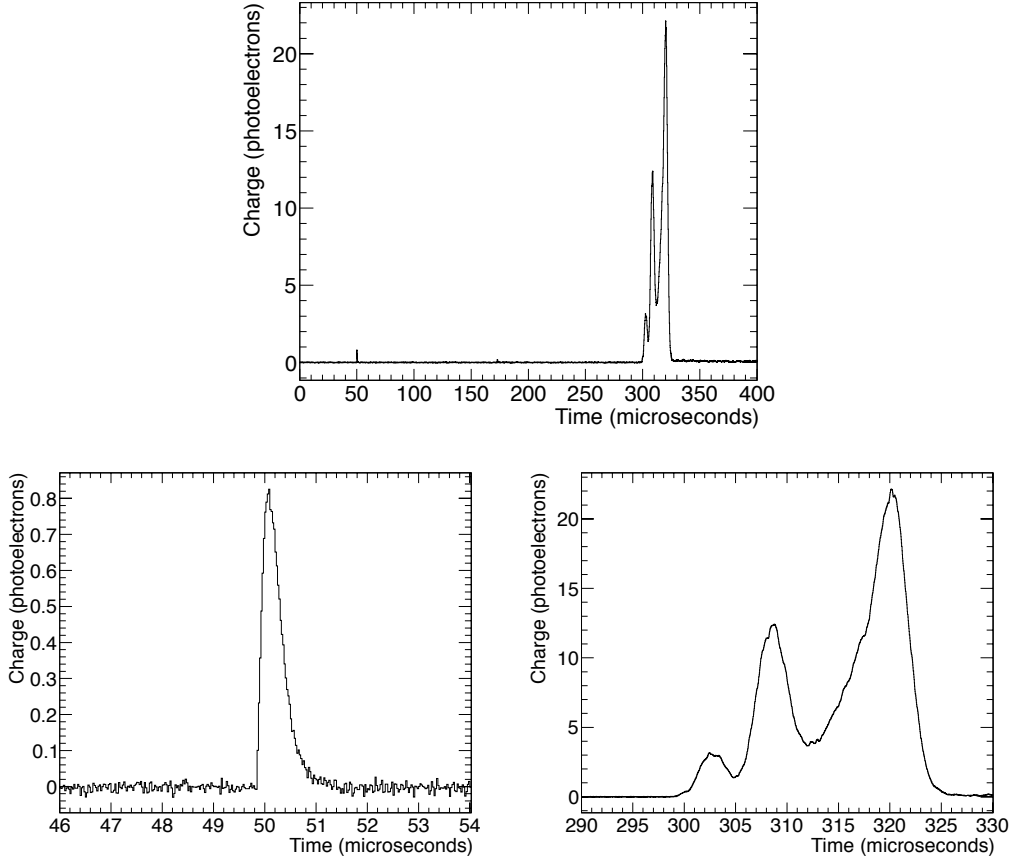


Figure 12. Top: Typical waveform of a 511-keV gamma-ray event obtained by summing the pedestal-subtracted, gain-corrected signals of the energy plane (and dividing by the number of PMTs, 19). Bottom: Close-up of the S1 (left) and S2 (right) pulses in the above waveform. The time difference between the leading edges of these pulses indicates the drift time, and hence the longitudinal coordinate of the event. S1 pulses are typically shorter than $3\ \mu\text{s}$ (this width mostly due to the shaping of the front-end electronics) and have an average charge of at least $0.5\ \text{pe/PMT}$, whereas S2 peaks are longer than $3\ \mu\text{s}$ and their integrated charge is at least $10\ \text{pe/PMT}$.

waveforms were converted from ADC counts to photoelectrons (*pes*). Third, the 19 waveforms of the energy-plane PMTs were summed together. This summed waveform (see figure 12, top), which is less affected by statistical fluctuations and (uncorrelated) noise, was then resampled from 40 MHz (the sampling rate of the electronics) to 1 MHz and scanned with a pulse-finding algorithm to extract its features. This algorithm builds pulses (or *peaks*) as collections of consecutive samples rising above the baseline. The found peaks were classified as S1-like or S2-like according to their duration and area (integrated charge). Peaks were considered S1-like (figure 12, bottom left) if their width was less than $3\ \mu\text{s}$ and their total charge was at least $0.5\ \text{pe/PMT}$, whereas peaks classified as S2-like (figure 12, bottom right) were at least $3\ \mu\text{s}$ wide and had a minimum integrated charge of $10\ \text{pe/PMT}$.

Events without an S1-like peak or with more than one were discarded at this stage. Events were also rejected if the S1 was not synchronized within a $50\ \mu\text{s}$ wide window with the NaI signal. For

the BC data this check was redundant because the detector had been triggered on that coincidence, but it was kept nonetheless so that both data sets were processed with the same offline algorithms.

4. Primary signals in NEXT-DEMO

Charged particles interacting with the xenon gas lose their energy through two different atomic processes: *excitation* and *ionization*. Both the atomic de-excitations and the recombination of ionization pairs lead eventually to the emission of (primary) scintillation light with a wavelength spectrum that peaks in the vacuum ultraviolet, around 172 nm. Several measurements of the average energy spent in the creation of one primary scintillation photon, W_{sci} , have been reported for xenon gas: 72 ± 6 eV [7], 111 ± 16 eV [8] and 76 ± 12 eV [9]. These measurements were done with drift fields of about 0.5 kV/cm and gas pressures in the range between 1 and 20 bar. The error-weighted mean is $W_{\text{sci}} = 77 \pm 5$ eV, and hence an electron of energy $E = 511$ keV produces in average $N_{\text{sci}} = E/W_{\text{sci}} = (6640 \pm 430)$ scintillation photons. In practice, however, only a small fraction of these photons is detected due to the finite photocathode coverage of any detector and the inefficiencies in the collection of light.

The average energy spent in the creation of an ionization pair is $W_{\text{ion}} = 22.0$ eV [10]. The number of ionization pairs created on average by an electron of 511 keV is therefore $N_{\text{ion}} = 23\,227$. The statistical fluctuations of this number are smaller than those expected from a Poisson distribution, as described by Fano's theory [11]. Specifically, the variance of N_{ion} can be expressed as

$$\sigma_{\text{ion}}^2 = F N_{\text{ion}}, \quad (4.1)$$

where $F = 0.15$ [4] is the so-called *Fano factor* of xenon gas. Therefore the lowest achievable energy resolution measuring the ionization of xenon is

$$\delta E/E = 2.35 \sqrt{F W_{\text{ion}}/E}. \quad (4.2)$$

Under the influence of the electric field applied to the detector, the ionization electrons drift towards the anode at a velocity of about 1 mm/ μ s [12], while positive ions drift towards the cathode. Some of the electrons may be absorbed by electronegative impurities in the gas before reaching the anode. This process can be described by a negative exponential:

$$N(t_D) = N_0 \cdot \exp(-t_D/\tau), \quad (4.3)$$

where t_D is the drift time and τ is the mean *electron lifetime* in the gas. In addition, during the drift electrons spread gaussianly in both the longitudinal and transverse directions. This process, known as *diffusion*, limits the position resolution of gaseous detectors.

Once the primary electrons reach the EL region, they are accelerated between two parallel meshes giving rise to secondary scintillation (or electroluminescence). The number of photons emitted per primary electron and per unit of drift length and pressure, the so-called *reduced electroluminescence yield*, is linearly proportional to the reduced electric field E/p above a threshold of about 0.83 kV cm⁻¹ bar⁻¹ and up to ~ 6 kV cm⁻¹ bar⁻¹ [13]:

$$\frac{Y}{p} = 140 \frac{E}{p} - 116 \text{ [photons electron}^{-1} \text{ cm}^{-1} \text{ bar}^{-1}] \quad (4.4)$$

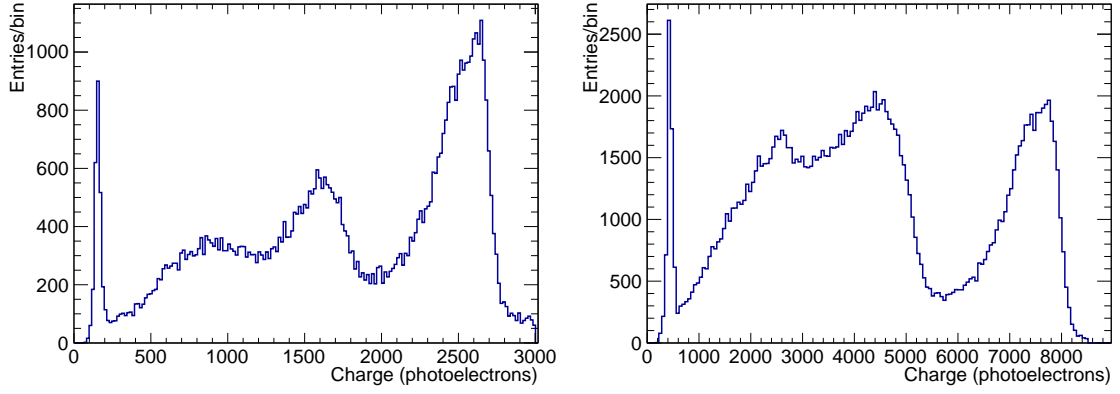


Figure 13. Raw energy spectrum — defined as the total integrated secondary-scintillation (S2) charge measured by the energy plane divided by the number of PMTs — recorded in NEXT-DEMO for the *ultraviolet* (left panel) and *blue* (right panel) configurations. From left to right in the spectra, the xenon x-ray peak, the Compton edge and the full energy peak are clearly visible in spite of the mediocre energy resolution before corrections. The discrepancy between the two spectra in the relative size of the Compton edge and the photoelectric peak is due to the different configuration of the detector trigger for the two periods.

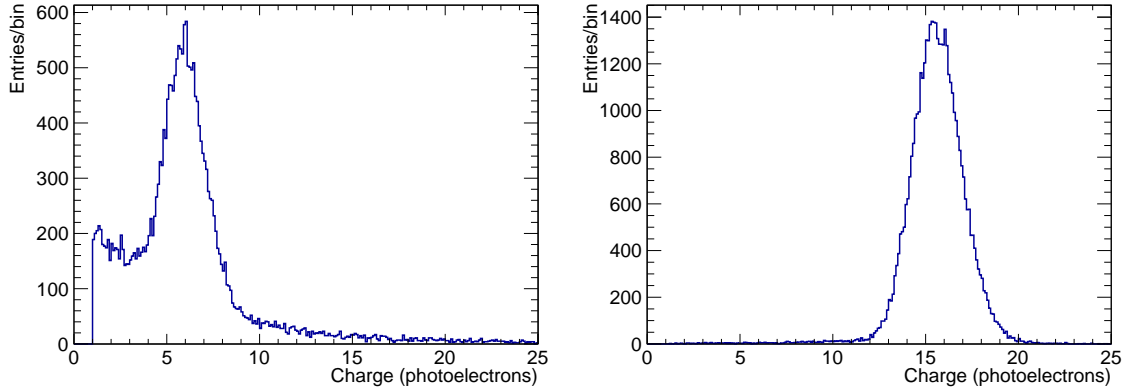


Figure 14. Intensity of the primary scintillation (S1) signal — i.e., integrated charge of the S1 peak of the energy-plane summed waveform — per PMT for photoelectric (full-energy) events. Left, for the *ultraviolet* configuration; right, for the *blue* configuration.

The fluctuations associated with the electroluminescence production are much smaller than the Fano factor, and hence the energy resolution of the detector is attributed only to the fluctuations in the ionization and in the photon detection system [4, 14].

In NEXT-DEMO the width of the EL region (delimited by the gate and anode meshes) is 0.5 cm, and for both the UVC and BC periods the operating pressure was 10 bar and the voltage across the grids was 12 kV. These parameters correspond to a reduced electric field of $2.4 \text{ kV cm}^{-1} \text{ bar}^{-1}$, or equivalently, according to equation (4.4), 1 100 photons per primary electron emitted across the EL region of NEXT-DEMO.

As mentioned in section 1, the energy plane of NEXT-DEMO detects a fraction of the secondary scintillation to provide a precise measurement of the total energy deposited in the chamber. More precisely, the energy of an event is defined as the total integrated charge (area) of all the S2 peaks

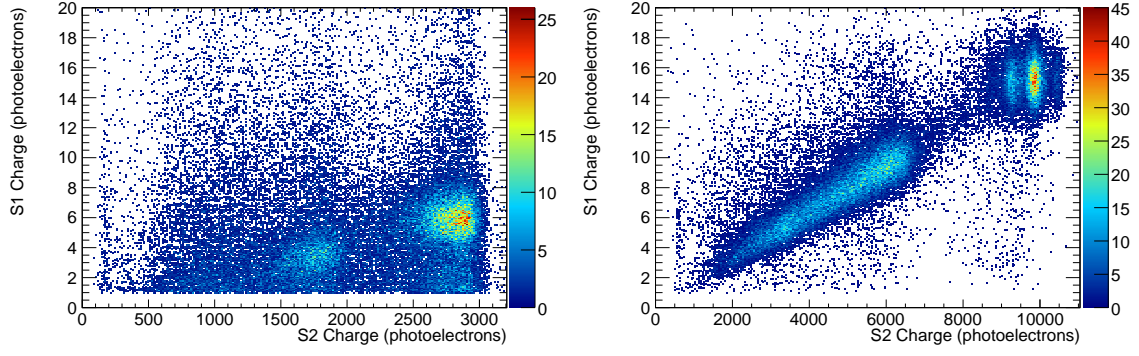


Figure 15. Correlation between the total integrated charge (per PMT) of the S1 and the S2 signals (after spatial corrections). Left, for the *ultraviolet* configuration; right, for the *blue* configuration. The island of full-energy events shows no indication of correlated fluctuations between S1 and S2.

in the summed waveform of the energy plane. Figure 13 shows the raw energy spectrum recorded in the chamber for both considered configurations. The xenon x-ray peak at low energy is clearly visible, as well as the Compton spectrum and the full-energy photoelectric peak. The improvement in light collection with the use of a TPB-coated light tube is noticeable, about a factor of 3 more photoelectrons. This is also apparent in the S1 signal, as shown in figure 14. We attribute the enhancement in light collection to two factors: the higher quantum efficiency of the PMTs at the wavelength of emission of TPB (~ 430 nm) and the near-perfect reflectivity of PTFE for the blue region of the electromagnetic spectrum [5].

Figure 15 shows the correlation between the S1 and S2 signals (after spatial corrections; see section 5) for both the UVC and BC. Notice that the island of full-energy (photoelectric) events shows no indication of correlated fluctuations between S1 and S2, like those observed with alpha particles [12] or in liquid xenon [15].

5. Energy resolution analysis

The data of the raw energy spectrum shown in figure 13 are affected by several factors that contribute to degrade the intrinsic energy resolution of gaseous xenon. The most important of those factors, according to comparisons between data and Monte Carlo simulations, is the position-dependent response of the detector. In other words, the signal recorded by the energy plane for a given energy varies with the position of the events. However, as we will show in the following, this effect can be corrected, thus improving the resolution.

Consider an electron track in the TPC resulting from the interaction of a 511-keV gamma ray, and assume that the true coordinates xyz of the associated S2 peaks can be determined. We define then E_{rec} , an estimator of the true energy of the event, as the product of the measured energy E_{obs} and a certain *detector response function* η :

$$E_{\text{rec}} = E_{\text{obs}}(x, y, z) \cdot \eta(x, y, z) \quad (5.1)$$

The obvious problem with this definition is that the true position of the event is not known. Instead, we measure a reconstructed position $x'y'z'$. The longitudinal position z' is calculated with

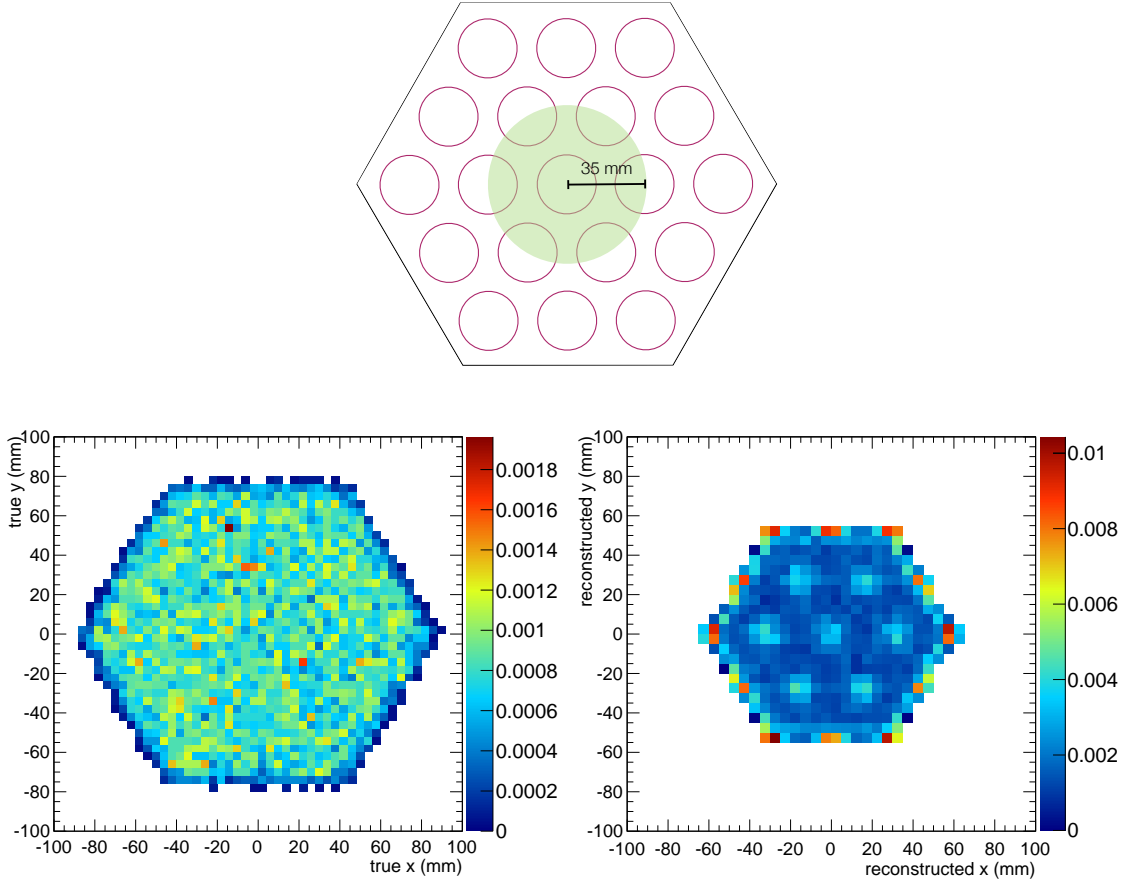


Figure 16. Top: Sketch of the NEXT-DEMO tracking plane showing the position of the photomultipliers (magenta circumferences) and the defined fiducial volume (green circle). Bottom: True average position (left panel; see text for definition) of simulated events compared to the reconstructed position (right panel) using the barycenter of the tracking plane. The original uniform distribution of events gets distorted, with events accumulating at the center of the PMTs and in a region intermediate between the first and second rings of sensors.

very good precision multiplying the drift time — defined as the time difference between the leading samples of the S1 and the S2 peaks — by the *drift velocity*, measured to be about $1 \text{ mm}/\mu\text{s}$ [12]. The transverse coordinates x and y are calculated as the signal-weighted average (*barycenter*) of the positions of the tracking-plane PMTs:

$$x' = \frac{\sum_i A_i x_i}{\sum_i A_i}, \quad y' = \frac{\sum_i A_i y_i}{\sum_i A_i}, \quad (5.2)$$

where A_i is the integrated charge of the S2 (area under the pulse) measured by PMT i , which is positioned at $x_i y_i$. We define as well a radial coordinate for the S2 peak as

$$R' = \sqrt{x'^2 + y'^2}. \quad (5.3)$$

Notice that we are assigning a single position to each S2 peak, and thus assuming that the associated tracks are point-like. This approximation is only acceptable if the detector response

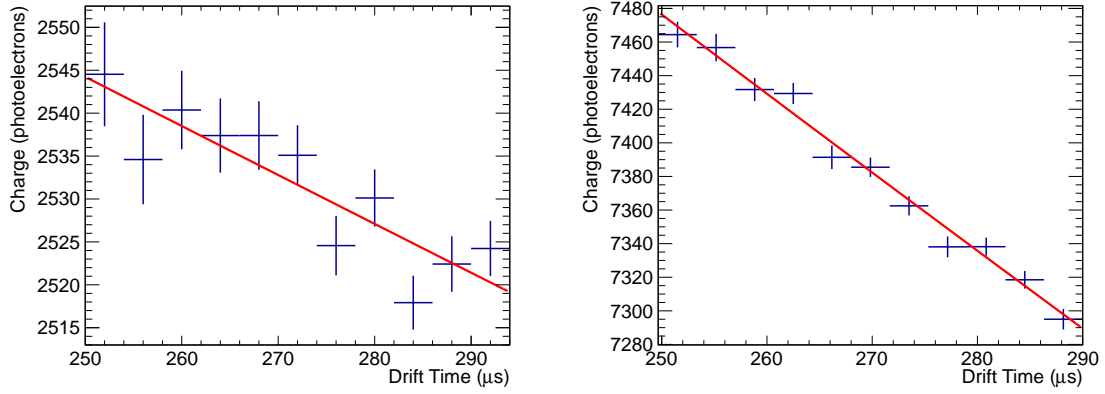


Figure 17. Dependence of the total integrated charge (energy) on drift time for photoelectric events. Left, for the *ultraviolet* configuration (UVC); right, for the *blue* configuration (BC). An exponential fit (red line) to the data determines the electron lifetime in the gas, obtaining 4.0 ms for the UVC and 1.7 ms for the BC.

function, η , does not vary appreciably between the farthest points of the track. In our case, the average range of a 511-keV electron in HPXe at 10 bar is 55 mm, but due to multiple scattering the effective size of the tracks is usually smaller, about 20 mm. Moreover, as section 6 explains, the energy is not uniformly distributed along the track — a small region of about 1 cm size concentrates $\sim 80\%$ of the energy of the 511-keV electron tracks. Therefore we conclude that for our data the single, energy-weighted position of the S2 peak can be used for the correction of the spatial effects. More energetic (and thus longer) tracks would have to be segmented and a different correction applied to the resulting sections.

Given the limited number of sensors in this configuration of the tracking plane, the barycenter is necessarily biased towards the center of the PMTs and towards small R . For instance, the barycenter of an S2 peak with a true xy position coincident with the outer ring of PMTs (see figure 16, top) is pulled towards the center by the inner ring of sensors because there is no other ring at higher radius to compensate its weight. This effect is illustrated in figure 16 (bottom), where the reconstructed $x'y'$ position of simulated 511-keV electron tracks is compared to their true (energy-weighted) xy position, showing the distortion introduced by the barycenter on a uniform distribution of events. Consequently, since the reconstructed position is not a good estimator of the true position for large radii, the first step in this analysis is the selection of events with $R' < 35$ mm, which corresponds to the position of the first ring of PMTs (see figure 16, top).

Next, we express the detector response function as the product of three terms:

$$\eta(x, y, z) = Z(z') \cdot \rho(R') \cdot \Phi(\phi'), \quad (5.4)$$

where $Z(z')$ is a function that depends only on the reconstructed longitudinal coordinate, $\rho(R')$ is a function that depends only on the reconstructed radius R' , and $\Phi(\phi')$ is a function that depends only on the reconstructed azimuthal coordinate $\phi' = \tan^{-1}(y'/x')$. Obviously, this definition is only correct if the correlations between the three corrections are small.

Figure 17 shows the dependence of the total integrated charge on the longitudinal coordinate (expressed, in this case, as drift time) for full-energy (photoelectric) events in the interval $[250, 290]$ μs . We cut on 290 μs to stay away from the edge effects of the cathode, located at 300 μs , and below

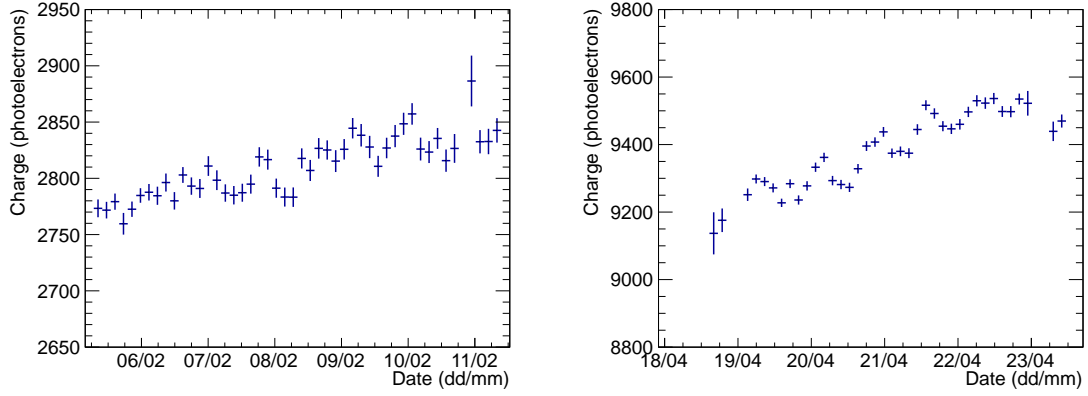


Figure 18. Evolution of the average S2 charge of the photoelectric peak during the data-taking period for both the UVC (left) and the BC (right).

250 μ s there is considerably less statistics due to the position and collimation of the calibration source. The longitudinal correction, described by equation (4.3), can be determined directly from the data by fitting them to a negative exponential. The fit yields the electron lifetime in the gas, τ : 4.0 ± 0.4 ms for the UVC and 1.7 ± 0.4 ms for the BC. The longer lifetime measured for the UVC indicates that during that period a higher gas purity was achieved. This was probably due to the micro-leak that appeared during the BC (see section 3) and the introduction of new (not clean) gas in the system to account for the losses. In any case, as proven by figure 18, the electron lifetime improved during both runs thanks to the continuous recirculation of the gas through the purification filters.

The radial correction — that is, the term $\rho(R')$ in equation (5.4) — is computed numerically by fitting a spline function to the profile histogram (figure 19, top left panel) showing the dependence of the energy on the reconstructed radius for photoelectric events, and normalized to the value for $R = 0$. The correction is then applied event by event. The result can be seen in the top right panel of figure 19. The azimuthal correction, $\Phi(\phi')$, is calculated the same way using the already R-corrected data — see the bottom panels of figure 19.

Finally, figure 20 shows the corrected energy spectrum of the 511-keV gamma rays from ^{22}Na in the fiducial volume of NEXT-DEMO for the two studied configurations. A gaussian fit to the photoelectric peak indicates an energy resolution of 2.89% FWHM for the UVC and 1.75% FWHM for the BC. The better energy resolution of the BC period is explained by the improved photoelectron statistics, which is a factor of three larger than in the UVC. Extrapolating the BC result to the Q value of ^{136}Xe (2458 keV) assuming a $E^{-1/2}$ dependence, we obtain a resolution of 0.8% FWHM, better than the NEXT target resolution of 1% FWHM at $Q_{\beta\beta}$.

6. The topological signature

Electron tracks in HPXe are tortuous due to multiple scattering and have a distinctive energy deposition pattern with a roughly constant dE/dx except at the end, where it increases by a factor of 4 to 5, leaving a large deposition that we call *blob*. This topological signature can be used in the search for $\beta\beta 0\nu$ to distinguish between signal (two electron tracks with a common vertex)

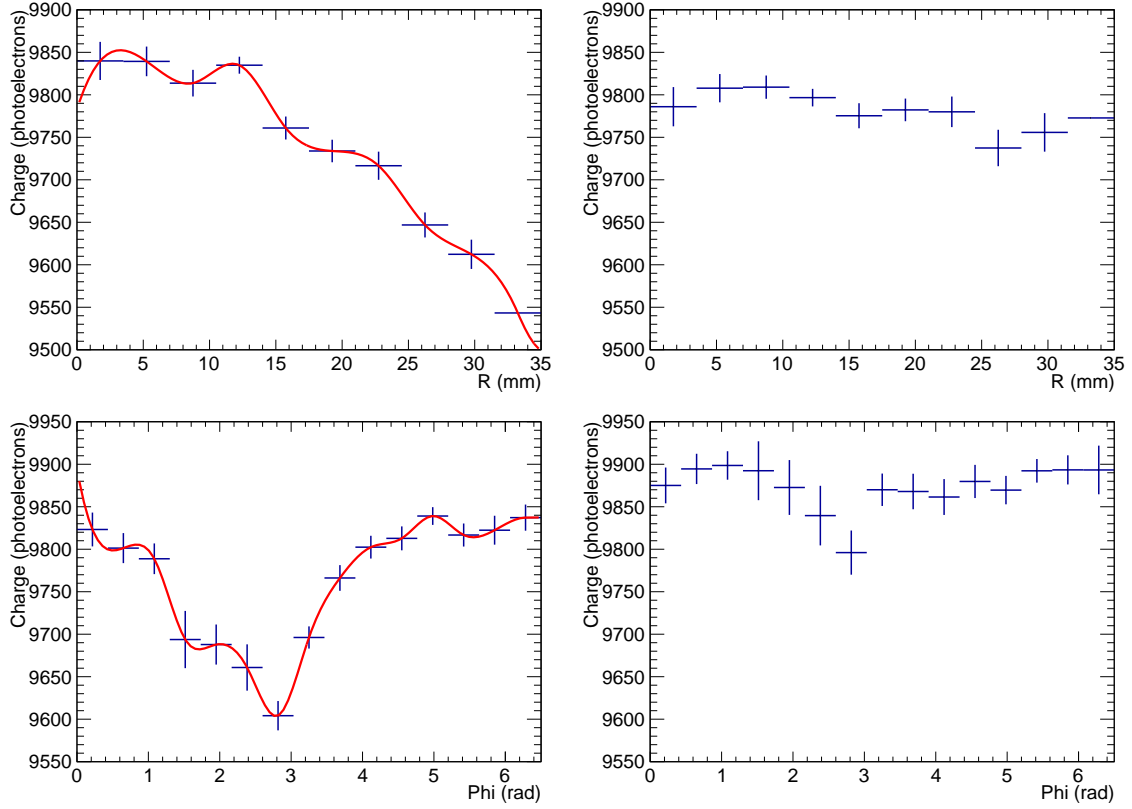


Figure 19. Radial (top panels) and azimuthal (bottom panels) corrections to the signal recorded by the NEXT-DEMO energy plane under the *blue* configuration. The correction is described by a spline fitted to the data (left panels), and then applied to the data event by event (right panels).

and background (mostly single electrons originated in the interaction of high-energy gammas), as demonstrated in the Gotthard experiment [16].

We present here a study (using the UVC data after spatial corrections) of the energy deposition pattern along z , taking advantage of the excellent spatial resolution in that coordinate. The ultimate algorithm exploiting the topological signature of NEXT will, of course, perform a full three-dimensional reconstruction of the tracks combining information from both detection planes, but, as we will see in the following, there is already important information that can be extracted from a simple analysis like this.

During the initial data processing, described in section 3.2, the individual waveforms of the energy-plane photomultipliers were summed together and resampled to 1 MHz (1 sample per microsecond). Each time sample, or *slice*, of this summed waveform corresponds then to 1 mm along the z coordinate. Figure 21 (left panel) shows the average number of slices that compose an S2 peak as a function of its total integrated charge. Above 600 photoelectrons the number of slices in the peak — and thus the length of the associated track — increases linearly, with a small change in the slope at 1 200 pe. The average number of slices for full-energy tracks is of the order of 20, that is, 2 cm along the longitudinal coordinate. Below 600 pe the average is affected by larger statistical fluctuations, given the small number of events in that zone of the energy spectrum.

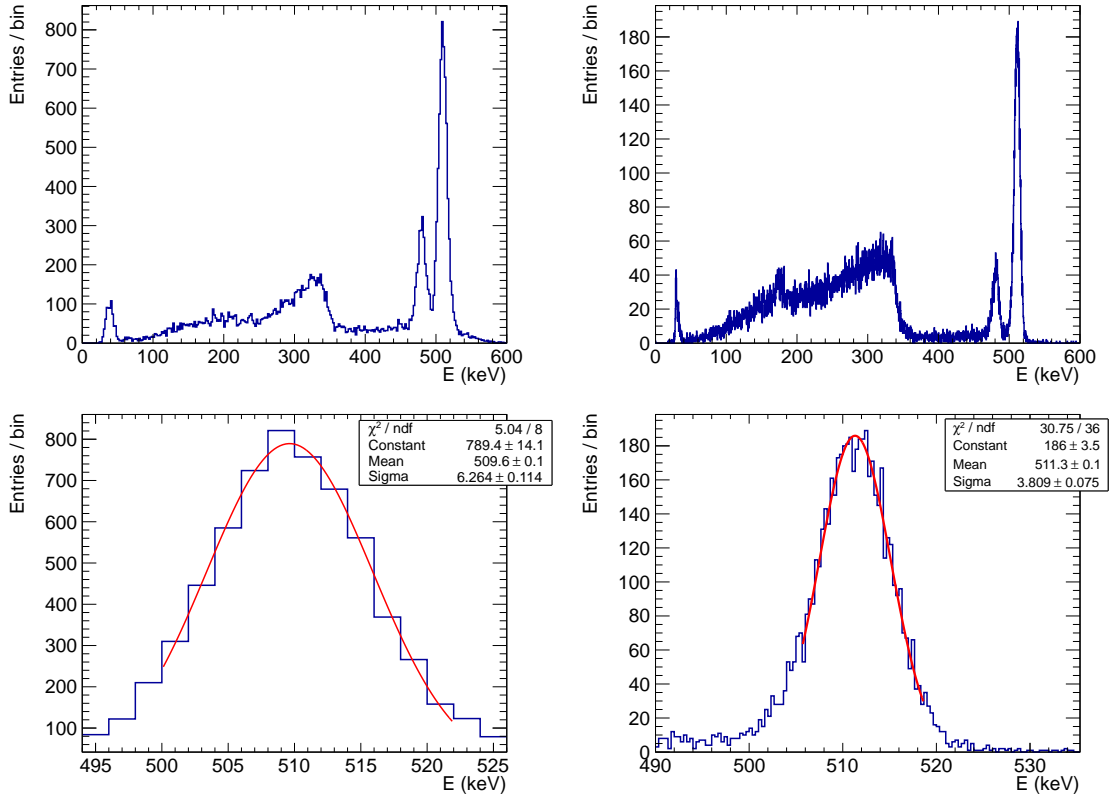


Figure 20. Top: Energy spectra for ^{22}Na gamma-ray events within the fiducial volume of NEXT-DEMO after spatial corrections. Left for the *ultraviolet* configuration (UVC); right for the *blue* configuration (BC). Bottom: Gaussian fits to the photoelectric peaks of the above energy spectra, indicating an energy resolution at 511 keV of 2.89% FWHM for the UVC and 1.75% FWHM for the BC.

Anyhow, the number of slices varies between 8 and 12. These widths are due to the gaussian spread of the ionization electrons caused by diffusion during the drift, because at those energies the tracks, with a mean range of less than 5 mm, are close to true point-like events. For tracks drifting ~ 30 cm, the sigma of the distribution is of the order $1.5 \mu\text{s}$ [12].

Figure 21 (right panel) shows the average energy of the slices as a function of the time difference with respect to the slice with maximum energy in 511-keV photoelectric events. A 10-slices wide peak concentrates $\sim 80\%$ of the energy, while the long tails have more than 10 times less energy per slice. The two parts correspond to the blob and the dE/dx constant sections of the electron track respectively. From this, a simple definition for the blob in a track can be formulated: a slice with an energy of at least 300 pes and whose neighbour slices have an energy greater than 50 pes. In 98% of the full-energy tracks a slice fulfilling that criterion was found, with only 0.14% of the cases finding two or more.

Figure 22 shows the relative position of the blob along its track — defined as the number of the slice with maximum energy divided by the total number of slices — for four different lengths of tracks. The blob is centered in the track when the number of slices is low, below 16. These are tracks where the electron probably spiraled due to multiple scattering, describing an almost closed trajectory. As the number of slices increases, the blob moves to the left. The bias in direction is

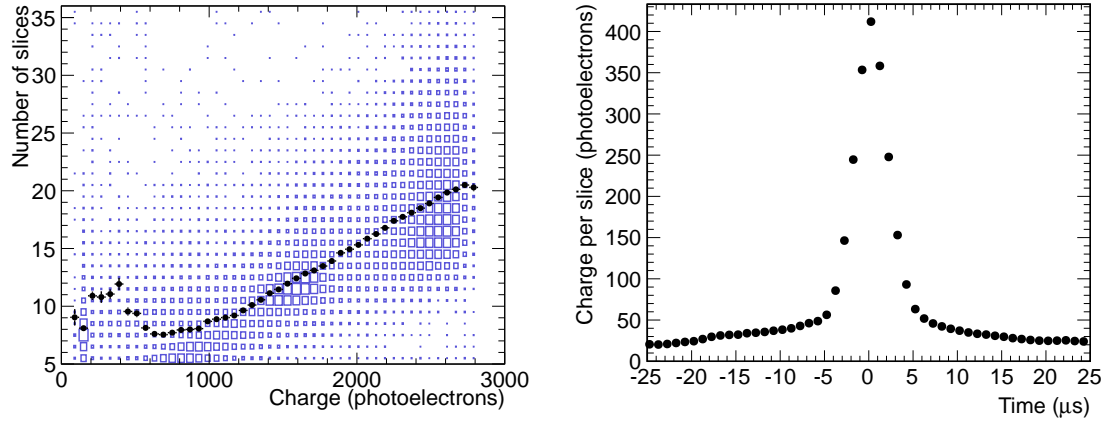


Figure 21. Left: Number of longitudinal slices in an S2 peak as a function of its integrated charge (energy). The average number (black dots) is superimposed on the 2D histogram (blue boxes). Right: Time-ordered distribution of slices with respect to the most energetic one for photoelectric events.

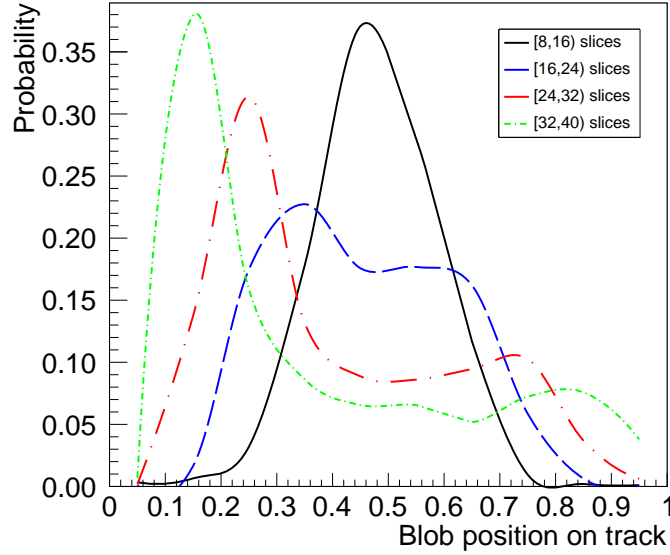


Figure 22. Relative position of the slice of maximum energy along the slices for different number of slices.

due to the fact that most tracks were produced close to the cathode (because of the position and collimation of the calibration source), and only those electrons moving towards the anode (to the left) are contained in the active volume, whereas those moving in the opposite direction are lost.

7. Summary and outlook

We have presented the initial results of the NEXT-DEMO detector operated with a tracking plane equipped with photomultiplier tubes and running under two configurations: one with a light tube made of PTFE panels surrounding the active volume, and another in which the PTFE panels have

been coated with tetraphenyl butadiene (TPB), a wavelength shifter. The detector response was studied with a ^{22}Na source. The notable increase in the recorded signals after coating — about a factor of 3 difference for the same energy — and the consequent improvement in energy resolution demonstrate the rationale behind the use of TPB.

The energy spectrum of electrons produced by the interacting 511 keV gammas in the gas has been reconstructed in a cylindric fiducial volume of 35 mm radius. The best resolution obtained, extrapolated to $Q_{\beta\beta}$, is 0.8% FWHM, improving the target defined in our TDR [1] of 1% FWHM at $Q_{\beta\beta}$, in spite of the simplicity of the corrections applied to the data. The measured electron lifetime was long, of the order of several milliseconds, showing that the gas recirculation through hot getters, as foreseen for NEXT-100, effectively removes the electronegative impurities from the gas.

Initial studies concerning the reconstruction of the topology, in particular the identification of the electron blob (the large energy deposit associated to the end of an electron track), have also been presented.

NEXT-DEMO is currently taking data with a tracking plane instrumented with SiPMs [17], and new results are under preparation.

Acknowledgments

This work was supported by the following agencies and institutions: the Ministerio de Economía y Competitividad of Spain under grants CONSOLIDER-Ingenio 2010 CSD2008-0037 (CUP) and FPA2009-13697-C04-04; the Director, Office of Science, Office of Basic Energy Sciences, of the US Department of Energy under contract no. DE-AC02-05CH11231; and the Portuguese FCT and FEDER through the program COMPETE, project PTDC/FIS/103860/2008. J. Renner (LBNL) acknowledges the support of a US DOE NNSA Stewardship Science Graduate Fellowship under contract no. DE-FC52-08NA28752.

References

- [1] **NEXT** Collaboration, V. Álvarez et al., *NEXT-100 Technical Design Report (TDR): Executive Summary*, *JINST* **7** (2012) T06001, [[arXiv:1202.0721](#)].
- [2] J. J. Gómez-Cadenas, J. Martín-Albo, M. Mezzetto, F. Monrabal, and M. Sorel, *The search for neutrinoless double beta decay*, *Riv. Nuovo Cim.* **35** (2012) 29–98, [[arXiv:1109.5515](#)].
- [3] J. J. Gómez-Cadenas, J. Martín-Albo, and F. Monrabal, *NEXT, high-pressure xenon gas experiments for ultimate sensitivity to Majorana neutrinos*, *JINST* **7** (2012) C11007, [[arXiv:1210.0341](#)].
- [4] D. Nygren, *High-pressure xenon gas electroluminescent TPC for $0\nu\beta\beta$ decay search*, *Nucl. Instrum. Meth. A* **603** (2009) 337–348.
- [5] C. Silva, J. Pinto da Cunha, A. Pereira, V. Chepel, M. Lopes, et al., *Reflectance of Polytetrafluoroethylene (PTFE) for Xenon Scintillation Light*, [arXiv:0910.1056](#).
- [6] S. Martoiu, H. Muller, and J. Toledo, *Front-end electronics for the Scalable Readout System of RD51*, in *Nuclear Science Symposium and Medical Imaging Conference (NSS/MIC)*, *IEEE*, pp. 2036–2038, 2011.
- [7] L. Fernandes et al., *Primary and secondary scintillation measurements in a xenon Gas Proportional Scintillation Counter*, *JINST* **5** (2010) P09006, [[arXiv:1009.2719](#)].

- [8] S. J. C. do Carmo, F. I. G. M. Borges, F. P. Santos, T. H. V. T. Dias, and C. A. N. Conde, *Absolute primary scintillation yield of gaseous xenon under low drift electric fields for 5.9 keV x-rays*, *JINST* **3** (2008) P07004,.
- [9] A. Parsons, T. Edberg, B. Sadoulet, S. Weiss, J. F. Wilkerson, et al., *High pressure gas scintillation drift chambers with wave shifter fiber readout*, *IEEE Trans. Nucl. Sci.* **37** (1990) 541–546.
- [10] S. P. Ahlen, *Theoretical and experimental aspects of the energy loss of relativistic heavily ionizing particles*, *Rev. Mod. Phys.* **52** (1980) 121–173.
- [11] U. Fano, *Ionization Yield of Radiations. 2. The Fluctuations of the Number of Ions*, *Phys. Rev.* **72** (1947) 26–29.
- [12] **NEXT** Collaboration, V. Álvarez et al., *Ionization and scintillation response of high-pressure xenon gas to alpha particles*, [arXiv:1211.4508](#).
- [13] C. Monteiro et al., *Secondary Scintillation Yield in Pure Xenon*, *JINST* **2** (2007) P05001, [[physics/0702142](#)].
- [14] C. A. B. Oliveira, M. Sorel, J. Martín-Albo, J. J. Gómez-Cadenas, A. L. Ferreira, et al., *Energy resolution studies for NEXT*, *JINST* **6** (2011) P05007, [[arXiv:1105.2954](#)].
- [15] **EXO** Collaboration, E. Conti et al., *Correlated fluctuations between luminescence and ionization in liquid xenon*, *Phys. Rev. B* **68** (2003) 054201, [[hep-ex/0303008](#)].
- [16] **Caltech-Neuchâtel-PSI** Collaboration, R. Luscher et al., *Search for $\beta\beta$ decay in Xe-136: New results from the Gotthard experiment*, *Phys. Lett. B* **434** (1998) 407–414.
- [17] **NEXT** Collaboration, V. Álvarez et al., *Design and characterization of the SiPM tracking system of the NEXT-100 demonstrator*, [arXiv:1206.6199](#).